



Article

A Simple Fabrication of $\text{Sb}_2\text{S}_3/\text{TiO}_2$ Photo-Anode with Long Wavelength Visible Light Absorption for Efficient Photoelectrochemical Water Oxidation

Fei Han ^{1,2,3}, Sai Ma ², Dong Li ^{2,*}, Md Mofasserul Alam ¹ and Zeheng Yang ^{1,*}¹ School of Chemistry and Chemical Engineering, Hefei University of Technology, Hefei 230009, China² School of Material Science and Engineering, North Minzu University, Yinchuan 750021, China³ Key Laboratory of Polymer Materials and Manufacturing Technology, North Minzu University, Yinchuan 750021, China* Correspondence: lidong@nun.edu.cn (D.L.); zehengyang@hfut.edu.cn (Z.Y.);
Tel.: +86-951-2067378 (D.L.); +86-551-62901451 (Z.Y.)

Abstract: An Sb_2S_3 -sensitized TiO_2 ($\text{Sb}_2\text{S}_3/\text{TiO}_2$) photo-anode (PA) exhibiting a high photo-electrochemical (PEC) performance in water oxidation has been successfully prepared by a simple chemical bath deposition (CBD) technique. Herein, the Raman spectra and XPS spectrum of $\text{Sb}_2\text{S}_3/\text{TiO}_2$ confirmed the formation of Sb_2S_3 on the TiO_2 coatings. The $\text{Sb}_2\text{S}_3/\text{TiO}_2$ photo-anode significantly shifted the absorption edge from 395 nm (3.10 eV) to 650 nm (1.90 eV). Furthermore, the $\text{Sb}_2\text{S}_3/\text{TiO}_2$ photo-anode generated a photo-anodic current under visible light irradiation below 650 nm due to the photo-electrochemical action compared with the TiO_2 photo-anode at 390 nm. The incident photon-to-current conversion efficiency (IPCE = 7.7%) at 400 nm and -0.3 V vs. Ag/AgCl was 37 times higher than that (0.21%) of the TiO_2 photo-anodes due to the low recombination rate and acceleration of the carriers of $\text{Sb}_2\text{S}_3/\text{TiO}_2$. Moreover, the photo-anodic current and photostability of the $\text{Sb}_2\text{S}_3/\text{TiO}_2$ photo-anodes improved via adding the Co^{2+} ions to the electrolyte solution during photo-electrocatalysis.

Keywords: $\text{Sb}_2\text{S}_3/\text{TiO}_2$; photo-anode; long wavelength; photo-electrochemical; water oxidation

Citation: Han, F.; Ma, S.; Li, D.; Alam, M.M.; Yang, Z. A Simple Fabrication of $\text{Sb}_2\text{S}_3/\text{TiO}_2$ Photo-Anode with Long Wavelength Visible Light Absorption for Efficient Photoelectrochemical Water Oxidation. *Nanomaterials* **2022**, *12*, 3444. <https://doi.org/10.3390/nano12193444>

Academic Editor: Barbara Vercelli

Received: 31 August 2022

Accepted: 28 September 2022

Published: 1 October 2022

Publisher's Note: MDPI stays neutral with regard to jurisdictional claims in published maps and institutional affiliations.



Copyright: © 2022 by the authors. Licensee MDPI, Basel, Switzerland. This article is an open access article distributed under the terms and conditions of the Creative Commons Attribution (CC BY) license (<https://creativecommons.org/licenses/by/4.0/>).

1. Introduction

PEC water splitting using semiconductors has been expected to be one of the ideal ways to realize the conversion of solar radiative energy into hydrogen energy [1–3]. In the PEC system, water oxidation is considered the kinetic control step of the whole water splitting process due to the sluggish kinetics of PEC water oxidation through photo-anodes (pAs). Therefore, developing a robust, stable, and economical photo-anode is critical for highly efficient solar water-splitting.

PEC water oxidation using n-type TiO_2 semiconductor pAs has gained considerable attention since 1972 due to their chemical and electrochemical stability in oxidation conditions, easy preparation, and noticeable incident light-to-current conversion efficiencies [4]. However, TiO_2 pAs-based PEC water oxidation is limited because of two serious drawbacks. First, TiO_2 has a wide bandgap (3.0–3.2 eV) that solely responds to the ultraviolet fraction of the solar spectrum (accounts for just 5% of solar irradiation) [5,6]. Second, a high recombination probability of electron-hole pairs leads to decreased incident light-to-current conversion efficiency.

Considering these disadvantages, developing highly active TiO_2 pAs is integral to absorbing solar irradiations from ultraviolet to visible light. So far, many efforts have been devoted to noble metal loading [7–10], semiconductor recombination [11–15], doping [16–19] and sensitization [13,19–30] to enlarge the spectral response range due to improve its PEC performance for efficient water oxidation and to promote electron-hole pair separation.

Among these, the sensitization of TiO₂ utilizing chalcogenide-based (Sb₂S₃) catalysts has received significant attention [19–21,31,32]. Sb₂S₃ possesses a suitable bandgap (1.6–1.9 eV) and a high absorption coefficient (105 cm⁻¹) in the visible region, which benefits from absorbing the whole visible and near-infrared range of the solar spectrum. Moreover, Sb₂S₃ has low toxicity and moisture, making it one of the most potential sensitizers to investigate the sensitization application. Due to these phenomena, Sb₂S₃/TiO₂ pAs were fabricated by a sensitization process with Sb₂S₃ as a sensitizer, exhibiting enhanced PEC water oxidation properties.

Meanwhile, different strategies have been noted for preparing the Sb₂S₃/TiO₂ pAs, such as atomic layer deposition (ALD), chemical bath deposition (CBD), successive ionic layer adsorption and reaction, etc. However, the costs associated with these physical methods are comprehensive. CBD has been selected in this article due to its low cost and simple procedure [33–36]. Moreover, several synthetic strategies need subsequent complex steps involving a somewhat complicated procedure for reproducible Sb₂S₃/TiO₂ and developing a simple and reproducible fabrication technique for Sb₂S₃/TiO₂ pAs synthesis. Herein, we describe a simple, low-cost, straightforward strategy for fabricating Sb₂S₃/TiO₂ pAs using a CBD technique. Sb₂S₃ were coated and deposited on the TiO₂ coated previously squeezed onto the ITO substrate utilizing a commercially available TiO₂ paste (PST-18NR). The Sb₂S₃/TiO₂ pAs show a higher PEC execution in water oxidation than TiO₂ pAs due to the charge separation and transportation acceleration phenomena.

2. Materials and Methods

2.1. Materials

Antimony (III) chloride (SbCl₃), Marpolose (60MP-50), HCl, and Polyethylene glycol (PEG, molecular weight = 2000) were purchased from Aladdin's Reagent (Shanghai Aladdin Bio-Chem Technology Co., Ltd., Shanghai, China) and TiO₂ paste (18 NR-T) was purchased from Macklin Reagent (Shanghai Macklin Biochemical Co., Ltd. Shanghai, China). An Indium tin oxide (ITO)-coated glass substrate was obtained from Dalian HepaChroma Co., Ltd., (Dalian, China); Millipore water (DIRECT-Q 3UV, Merck Ltd. Shanghai, China) was used for all the experiments. All other chemicals were of analytical grade and were used as received unless mentioned otherwise.

2.2. Fabrication of TiO₂/ITO Electrode

In a typical procedure, the TiO₂ pAs was synthesized as follows. Before coating, the FTO-glass substrate (1.0 cm⁻² area) was cleaned up using deionized water, acetone, and ethanol by sonication for 15 min. Then TiO₂ paste was squeezed over an ITO-glass substrate by a doctor-blade coater and dried at 80 °C for 15 min. After repeating the procedure twice, the electrode was calcined at 550 °C under an air atmosphere for 2 h to create a TiO₂ film-coated ITO electrode (TiO₂/ITO).

2.3. Fabrication of Sb₂S₃/TiO₂/ITO Electrode

SbCl₃ (787.1 mg, 3.46 mmol) was solved in acetone (3.03 mL); after the Na₂S₂O₃ (30.3 mL, 1 mol/L) solution was added, the Sb₂S₃ suspension was obtained. Then, the TiO₂/ITO was immersed into the resulting Sb₂S₃ suspension for 24 h in the refrigerator at 10 °C. The electrode was washed thoroughly with water and air-dried to obtain the Sb₂S₃/TiO₂/ITO electrode.

2.4. Measurement

A Shimadzu XRD-6000 diffractometer (Shimadzu International Trade (Shanghai) Co., Ltd., Shanghai, China) with Cu K α ($\lambda = 0.15406$ nm) radiation was utilized to determine the structure of samples and to obtain the X-ray diffraction (XRD) patterns. Raman microspectroscopic apparatus (Horiba-Jobin-Yvon LabRAM HR, Paris, France) was used to obtain the Raman spectra. At room temperature, a silicon reference sample was calibrated with a theoretical position of 520.7 cm⁻¹. The spectrophotometer (Shimadzu UV-2700, Shimadzu

International Trade (Shanghai) Co., Ltd., Shanghai, China) was used to test the UV–visible diffuse reflectance spectra (DRS). An electron probe microanalysis (JED-2300, JEOL, Tokyo, Japan) operating at 10 kV (acceleration voltage) was used to obtain the energy-dispersive X-ray spectroscopic (EDS) data. The XPS spectra were performed using a Thermo Fisher Scientific ESCALAB Xi+ instrument (Thermo Fisher Scientific (China) Co., Ltd., Shanghai, China) and calibrated in reference to C 1 s peak fixed at 284.2 eV.

All PEC measurements were examined using an electrochemical workstation in a single-compartment PEC cell (Shanghai Chenhua Instrument Co., Ltd. Shanghai, China, CHI760E). The prepared electrode was used as the working electrode. An Ag/AgCl electrode was used as the reference electrode, and a Pt wire as the counter electrode. An aqueous 0.1 M phosphate solution (pH 6.0) was used as an electrolyte in the cell compartments and Ar-gas environments. The cyclic voltammogram (CV) was recorded at a scan rate of 50 mV s^{-1} at room temperature. The output of light intensity was calibrated as 100 mW cm^{-2} using a spectroradiometer (USR-40, Ushio Shanghai Inc., Shanghai, China). Light ($\lambda > 500 \text{ nm}$, 100 mW/cm^2) was irradiated from an irradiation source of a 500 W xenon lamp (Optical Module X, Ushio Shanghai Inc., Shanghai, China) with a UV-cut filter ($\lambda > 500$), and a 0.2 M CuSO_4 was used as a liquid filter for cutting the heat ray. The linear sweep voltammograms (LSV) were measured at a scan rate of 5 mV s^{-1} . A monochromatic light with a 10 nm bandwidth was used with a 500 W xenon lamp using a monochromator for incident photon-to-current conversion efficiency (IPCE) measurements.

Photo-electrocatalysis was executed under the potentiostatic conditions at -0.3 V at $25 \text{ }^\circ\text{C}$ with the illumination of light ($\lambda > 500 \text{ nm}$, 100 mW/cm^2) for 1 h. 0.1 mM $\text{Co}(\text{NO}_3)_2 \cdot 6\text{H}_2\text{O}$ was dissolved in the electrolyte solution to test the effect of Co^{2+} ions on photo-electrocatalysis.

3. Results

3.1. Optimization of Immersion Time

The UV–vis absorption spectrum of $\text{Sb}_2\text{S}_3/\text{TiO}_2/\text{ITO}$ electrodes immersing at different times is shown in Figure 1a. No response was observed for the TiO_2/ITO electrode in the visible region. On the contrary, a dramatic response was observed for $\text{Sb}_2\text{S}_3/\text{TiO}_2/\text{ITO}$ electrodes, which are extended over the whole visible region (450–800 nm), demonstrating that the hole-electron pairs can be separated efficiently after sensitizing with Sb_2S_3 . Figure 1b shows the plots of the immersion times with the absorbance at 460 nm for the $\text{Sb}_2\text{S}_3/\text{TiO}_2/\text{ITO}$ electrodes. The absorbance exhibited an increasing tendency with immersion time increased; the highest absorbance was observed when the immersion time was 24 h. After that, the absorbance decreased when the immersion time increased, suggesting that the optimum immersion condition was 24 h, which was employed in the following experiments.

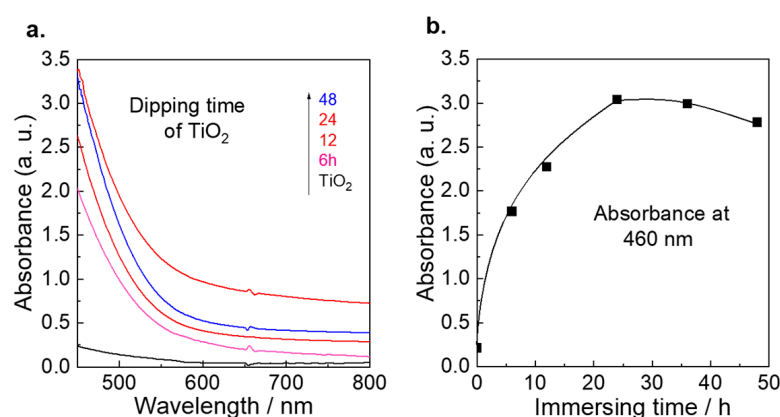


Figure 1. (a) UV–Vis spectral change of the $\text{Sb}_2\text{S}_3/\text{TiO}_2$ at difference time for dipping; (b) Plots of Absorbance vs. immersion time for $\text{Sb}_2\text{S}_3/\text{TiO}_2$, respectively.

3.2. Characterization Structure of Different Samples

The crystalline structures of the ITO, TiO₂ and Sb₂S₃/TiO₂ electrodes were characterized by XRD diffraction (Figure 2). Figure 2Ia shows the peaks of the ITO substrate. The diffracted peaks of TiO₂/ITO (Figure 2Ib) and Sb₂S₃/TiO₂/ITO electrodes (Figure 2Ic) were clearly detected at $2\theta = 25.1^\circ$, 37.7° , 47.8° , 53.9° and 53.9° , respectively (JSPDF number: 89–4921) [5]. No peaks in terms of Sb₂S₃ were observed for both electrodes. However, it should be noted that two slightly broadened peaks were detected around $2\theta = 12$ and 55° for the Sb₂S₃/TiO₂/FTO electrode. Raman spectroscopy was carried out for different powders scratching from the electrodes. Both TiO₂ (Figure 2IIb) and Sb₂S₃/TiO₂ (Figure 2IIc) samples exhibited the typical peaks located at 147, 199, 400, 517, and 638 cm⁻¹, which correspond to the vibrational modes of pure anatase TiO₂ [20,37]. Figure 2IIa shows the peak of 289 cm⁻¹ for Sb₂S₃, which could be assigned to the Sb-S stretching modes [20,31,38–40]. Moreover, this broad peak was observed in Sb₂S₃/TiO₂, while it was not detected for pure TiO₂ (Figure 2IIb), confirming the Sb₂S₃/TiO₂ composite formation.

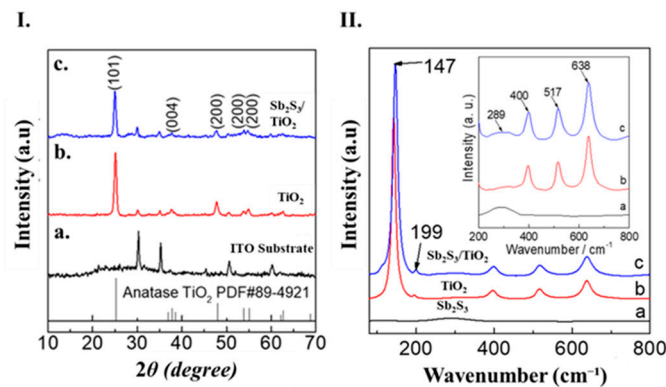


Figure 2. (I) X-RD data; (a) ITO substrate; (b) TiO₂, and (c) Sb₂S₃/TiO₂ photo-anodes, respectively; (II) Raman spectroscopy; (a) Sb₂S₃, (b) TiO₂, and (c) Sb₂S₃/TiO₂ powders, respectively.

The valence state of Sb₂S₃/TiO₂ was investigated utilizing XPS. As shown in the survey scan in Figure 3a, Sb, Ti, S, and O elements were verified. In the high-resolution Ti 2p spectrum (Figure 3b), two peaks at 458.8 and 464.5 eV were observed, assigned to the binding energies of Ti 2p_{3/2} and Ti 2p_{1/2} of the TiO₂ lattice, respectively [16,17,37]. The XPS spectrum of Sb₂S₃/TiO₂ exhibited two peaks in the S 2p region at 161.4 and 162.4 eV correspond to S 2p_{1/2} and S 2p_{3/2} of divalent S in Figure 3c [16,19,41]. The peaks at 529.3 and 538.7 eV in the Sb 3d region for Sb₂S₃/TiO₂, respectively, are assigned the Sb³⁺ oxidation state of Sb and are consistent with the earlier-reported values of Sb₂S₃ [19,42–44]. The relatively weak peak at 531.7 can be assigned to the formation of the Sb-O band at the surface, possibly associated with the oxygen atom of TiO₂.

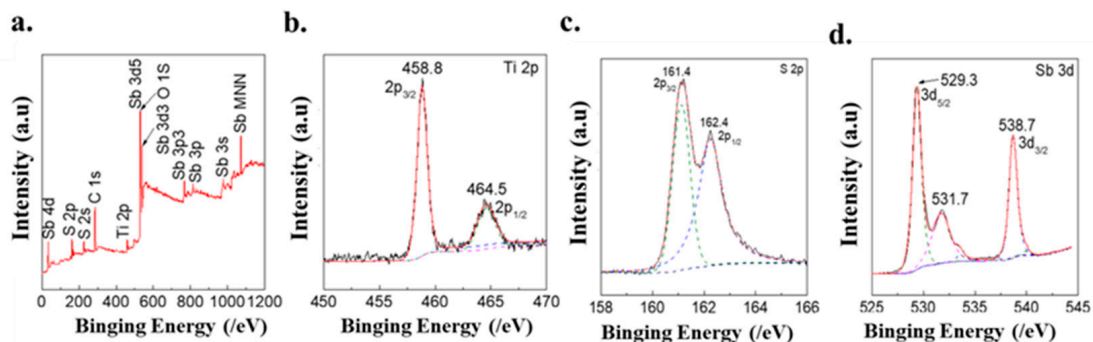


Figure 3. XPS spectra of the Sb₂S₃/TiO₂; (a) survey scan, (b) Ti 2p, (c) S 2p, and (d) Sb 3d, respectively. For the spectra in the Ti 2p, S 2p, and Sb 3d regions, the dashed lines are the deconvoluted spectrum bands, and the solid lines are the spectrum simulated by the deconvoluted bands.

The FE-SEM observed the morphologies of the TiO_2 and $\text{Sb}_2\text{S}_3/\text{TiO}_2$ electrodes. Figure 4I(a) exhibited the top view of the TiO_2 electrode at low magnification, in which a continuous uniform and smoothed surface were formed. This would be beneficial to improve the PEC performance of the $\text{Sb}_2\text{S}_3/\text{TiO}_2$ electrode due to accelerating the water oxidation reaction at the surface of the electrolyte solution. The FE-SEM images at high magnification (Figure 4I(b)) showed that the average particle size of TiO_2 was 10 nm. The surface FE-SEM image of the $\text{Sb}_2\text{S}_3/\text{TiO}_2$ electrode at low magnification is shown in Figure 4I(c), where the larger Sb_2S_3 particles were deposited on the TiO_2 surface. After that, the 60–100 nm Sb_2S_3 particles were clearly observed in Figure 4I(d). EDX analyses of the $\text{Sb}_2\text{S}_3/\text{TiO}_2$ electrode were taken to confirm the Sb_2S_3 deposition and complete the chemical composition information. The elemental maps of the EDX for the $\text{Sb}_2\text{S}_3/\text{TiO}_2$ electrode are shown in Figure 4II. The Ti and O mapping signals (Figure 4II(c,d)) and S and Sb (Figure 4II(e,f)) were detected. The distribution of Sb_2S_3 onto the TiO_2 in the $\text{Sb}_2\text{S}_3/\text{TiO}_2$ electrode appeared clearly.

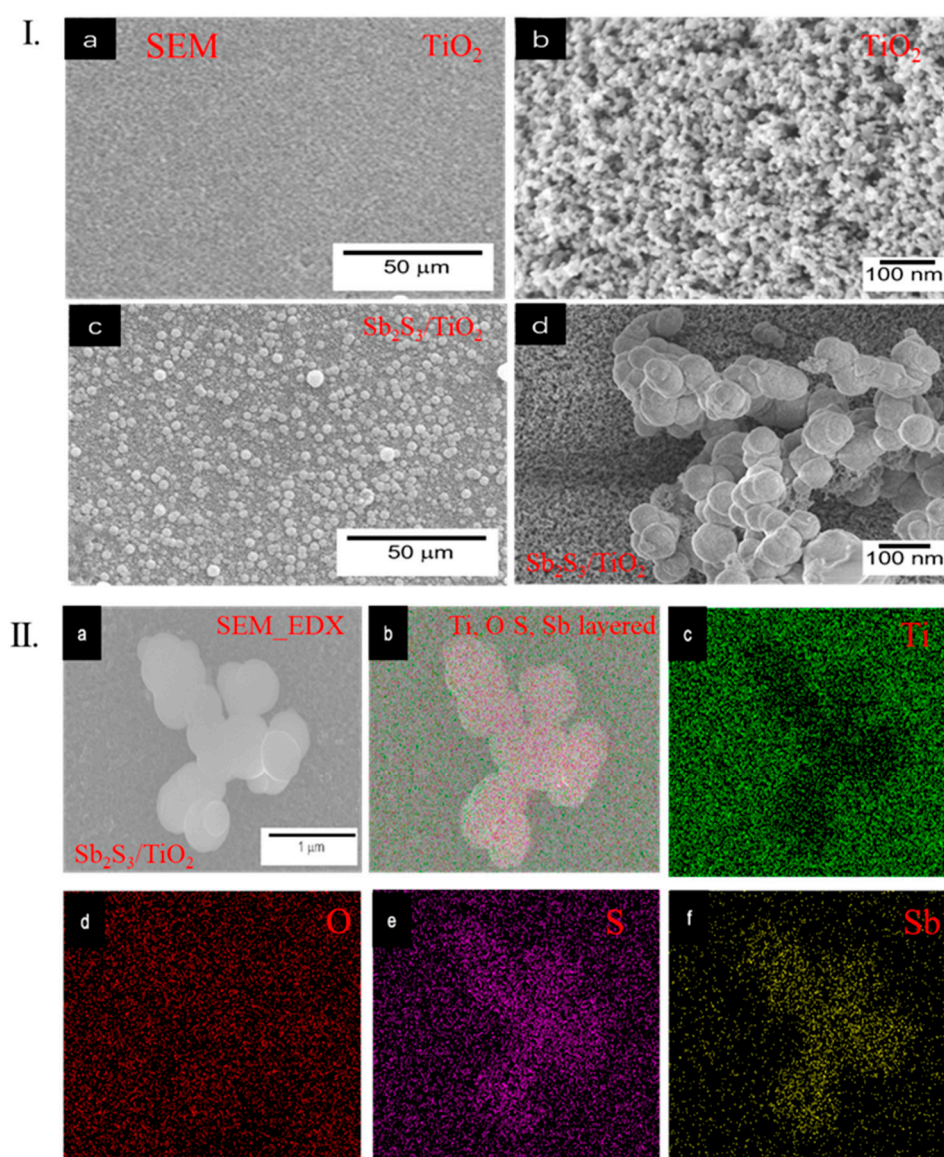


Figure 4. (I) SEM images; (a,b) TiO_2 and (c,d) $\text{Sb}_2\text{S}_3/\text{TiO}_2$ electrode, respectively; (II) (a) SEM_EDX elements distribution mapping images of the $\text{Sb}_2\text{S}_3/\text{TiO}_2$ electrode; (b) Ti, O S, Sb layered, (c) Ti, (d) O, (e) S, and (f) Sb, respectively.

3.3. The Optical Properties of Sb_2S_3/TiO_2

The diffuse reflection spectrum of TiO_2 and Sb_2S_3/TiO_2 are presented in Figure 5a. It was observed that the Sb_2S_3/TiO_2 absorb the visible light below 650 nm, exhibiting significant redshift in a broad wavelength region compared to TiO_2 (395 nm). Tauc plots based on UV-vis DRS are exhibited in Figure 5b. The TiO_2 showed a single absorption edge of 3.20 eV, corresponding to the previous report relating to anatase TiO_2 [5]. The Sb_2S_3/TiO_2 provided two different slopes due to the appearance of the new absorption edges, one of the band energies was 1.94 eV, and another was 2.37 eV. The photo-response of the Sb_2S_3/TiO_2 was significantly improved in the visible region. This is attributed to the existence of Sb_2S_3 , which significantly promotes the separation of the electron-hole pairs.

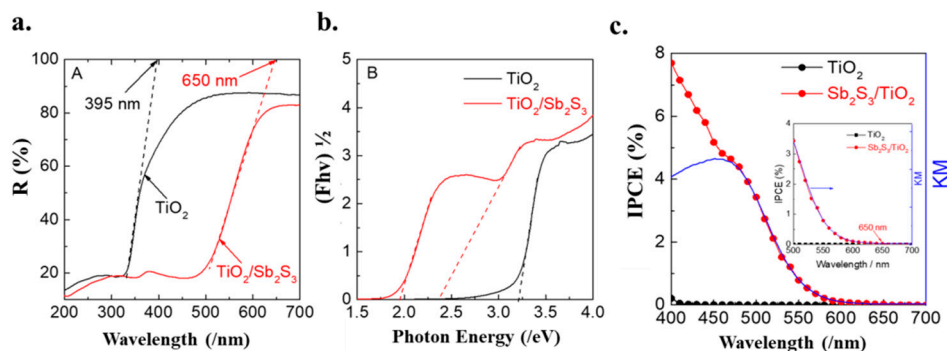


Figure 5. (a) Diffuse reflection spectrum of TiO_2 (black) and Sb_2S_3/TiO_2 (Red); (b) Tauc plots of TiO_2 (black) and Sb_2S_3/TiO_2 (red). The dashed lines show tangent lines near the edges of the plots, respectively, (c) Action spectra of IPCE of the TiO_2 (black) and Sb_2S_3/TiO_2 (red) electrode in a 0.1 M phosphate buffer solution of pH 6.0 at -0.3 V vs. Ag/AgCl. The insets show the magnified spectra near the edges.

3.4. Photoelectrocatalytic Properties

The action spectra of IPCE were recorded at -0.3 V by utilizing TiO_2 and Sb_2S_3/TiO_2 electrodes, as shown in Figure 5c. The IPCE value at 400 nm for Sb_2S_3/TiO_2 electrode (7.7%) is 37 times higher than that for TiO_2 electrode (0.21%). Further, the onset wavelength for photo-current generation on Sb_2S_3/TiO_2 electrode was 650 nm (1.9 eV), which is noticeably longer than the TiO_2 electrode (400 nm, 3.1 eV). The IPCE action spectra consisted of the UV-DRS data for Sb_2S_3/TiO_2 electrode, indicating that the pC was generated based on the bandgap excitation through collateral excitation from Sb 3d orbital to CB.

Several PEC examinations were performed to reveal the intrinsic PEC performances of TiO_2 and Sb_2S_3/TiO_2 electrodes towards water oxidation, as shown in Figure 6. Figure 6a showed the CV of the TiO_2 (black) and Sb_2S_3/TiO_2 (red) electrodes in a 0.1M phosphate solution (pH = 6.0). Both electrodes did not have photo-anodic currents in the dark condition (dashed line). Contrary to the TiO_2 electrode, which showed a 9.1 A/cm² at 0.2 V, the Sb_2S_3/TiO_2 electrode generated a stable photo-anodic current of 42.3 A/cm² based on water oxidation over 0.6 V, showing 4.6 times higher value than that of the TiO_2 electrode. Such remarkable enhancement of pC density for the Sb_2S_3/TiO_2 electrode can be ascribed to the improvement of light absorption in the visible region. The LSV of two electrodes shown in Figure 6b was taken under chopped/simulated chopped visible light irradiation. Interestingly, it can be observed that the photo-responses of anodic and cathodic currents for the Sb_2S_3/TiO_2 electrode (red) were clearly observed above or below -0.5 V, although hardly any pAs current was observed for the TiO_2 electrode (black, insert).

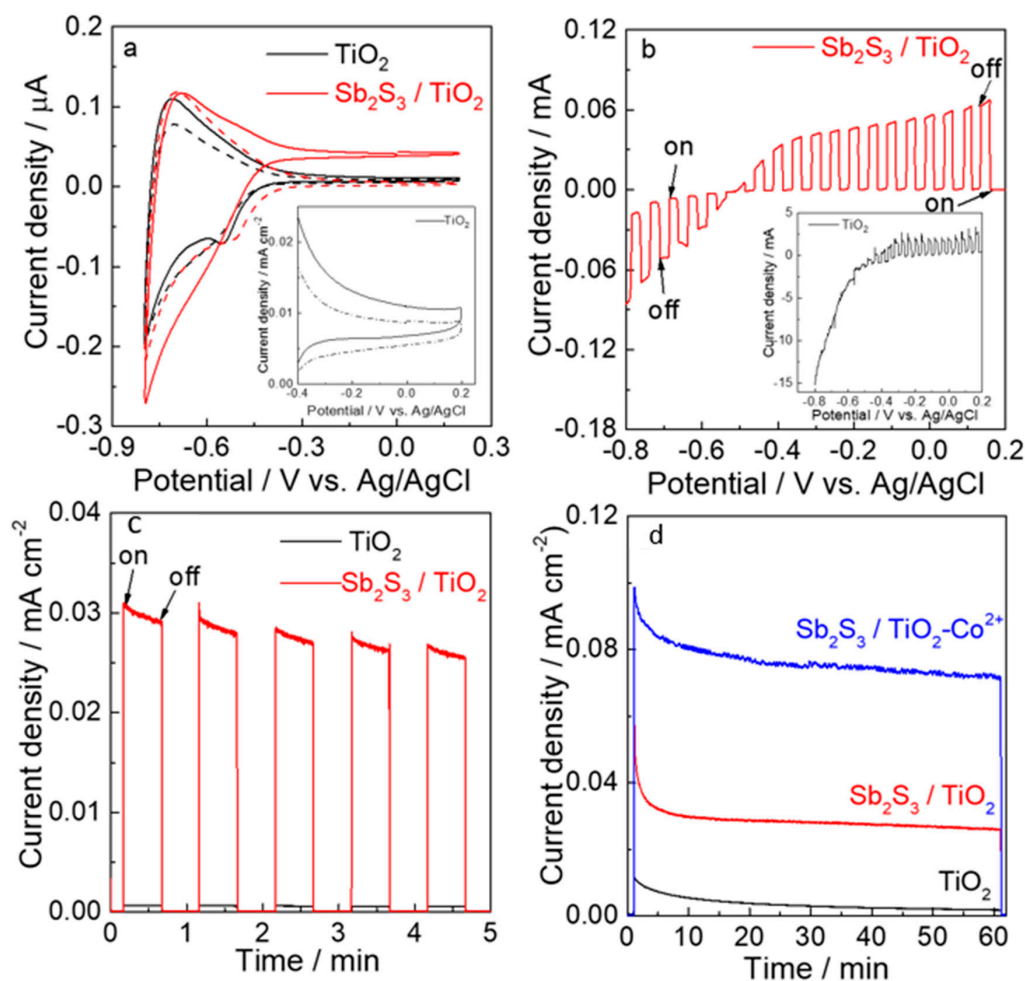


Figure 6. (a) CVs measured in the dark (dash) and on irradiation (solid); the subfigures in Figure 6a is the magnification from -0.4 V to 0.2 V for TiO_2 . (b) LSV plots and; (c) Transient on/off chopped photo-current response of the $\text{Sb}_2\text{S}_3/\text{TiO}_2$ (red) and TiO_2 (the subfigures in Figure 6b) photo-anode in a 0.1 M phosphate buffer solution of pH 7.0 with visible light irradiation ($\lambda > 500$ nm, 100 mW/cm²) chopped. (d) photo-current density-time profiles for $\text{Sb}_2\text{S}_3/\text{TiO}_2$ (red) and TiO_2 photo-anode (black) in 0.1 m phosphate buffer solution of pH 6.0 during photo-electrocatalytic water oxidation at -0.3 V vs. Ag/AgCl. $\text{Sb}_2\text{S}_3/\text{TiO}_2$ (blue) in the presence of 0.1 mM Co^{2+} ions in the electrolyte solution.

The results suggest that the photo-current direction of the $\text{Sb}_2\text{S}_3/\text{TiO}_2$ electrode can be modified according to the applied potential. When the potential is below -0.5 V, the charges separation based on bandgap excitation has caused upon irradiation with visible light, then the electrons from ITO are rapidly injected into the valence band of Sb_2S_3 through the conduction band of TiO_2 . Afterward, the electron acceptor in the conduction band of Sb_2S_3 is reduced by the electrons to generate a cathodic current. On the other condition of potential above -0.5 V, Sb_2S_3 absorbs photons to generate electron-hole pairs, the electrons are injected into the electron transport layer (TiO_2) and collected by ITO, and the holes oxidize the water at the surface of Sb_2S_3 to generate an anodic current. As the light was turned on and off, instantaneous positive and negative transient photocurrents were observed under chopper illumination at -0.3 V (Figure 6c).

A negligible photo-current for the TiO_2 electrode (black) was observed. However, the photo-current of 30 A/cm² for the $\text{Sb}_2\text{S}_3/\text{TiO}_2$ electrode (red) was observed. It is indicated that the charge carriers are very efficiently separated and limited to recombine after Sb_2S_3 sensitization. The photo-electrocatalysis was conducted under visible light irradiation ($\lambda > 500$ nm, 100 mW/cm²) at -0.3 V in a 0.1 M phosphate solution (pH = 6.0) for 1 h (Figure 6d). The I-t profile of the $\text{Sb}_2\text{S}_3/\text{TiO}_2$ electrode exhibited a photo-current

of 30 A/cm² over the period, while for the TiO₂ electrode, almost no photo-current was observed. The PEC performance of hematite and WO₃ photo-anodes for water oxidation can be enhanced by adding Co²⁺ ions into the electrolyte solution to act as catalysts at the electrode interface with the electrolyte solution without any deposition [45,46].

The influence of adding Co²⁺ ions on the PEC water oxidation for the Sb₂S₃/TiO₂ electrode was measured to prove this assumption. The performance of the Sb₂S₃/TiO₂ electrode for water oxidation was improved by the presence of 0.1 mM Co²⁺ ions in the phosphate buffer solution. It should be noted that the stability of the photo-current for the Sb₂S₃/TiO₂ electrode by the presence of Co²⁺ ions was remarkably improved, which consequently generated a 2.7 times higher photo-current of 80 A/cm² compared to the absence one. Such a lower decay rate (20%) of photo-current for the Sb₂S₃/TiO₂ electrode by the addition of Co²⁺ ions demonstrates that the stability is ascribed to the acceleration of the water oxidation reaction between the Sb₂S₃/TiO₂ surface and the electrolyte solution interface, which significantly reduce the recombination rate of photo-generated carriers.

4. Results and Discussion

Two main disadvantages are associated with high recombination of electron-hole pairs and a wide bandgap for TiO₂. Many efforts have been devoted to noble metal loading, semiconductor recombination, doping and sensitization to enlarge the spectral response range due to improving its PEC performance for efficient water oxidation and promoting electron-hole pairs separation. Sb₂S₃ possesses a suitable bandgap and a high absorption coefficient in the visible region, which benefits from absorbing the whole visible and near-infrared range of the solar spectrum. Thus, the Sb₂S₃/TiO₂ were fabricated by a sensitization process with Sb₂S₃ as a sensitizer, exhibiting enhanced PEC water oxidation properties. Herein, a simple, low-cost and straightforward strategy for fabricating Sb₂S₃/TiO₂ using a CBD technique was reported in this paper.

5. Conclusions

An Sb₂S₃/TiO₂ photo-anode was fabricated utilizing a simple and low-cost CBD strategy. XPS and elemental mapping detected Sb and S signals and Ti and O, demonstrating the formation of Sb₂S₃ and TiO₂, respectively. The Sb₂S₃/TiO₂ photo-anode can utilize visible light below 650 nm for PEC water oxidation, in contrast to utilization below 395 nm for the TiO₂ photo-anode. The IPCE of 7.7% at 400 nm for Sb₂S₃/TiO₂ photo-anode was higher than that of 0.21% for TiO₂ photo-anode by 37 times. The Sb₂S₃/TiO₂ photo-anode can generate a photo-anodic current and a photo-cathodic current in contrast to generating a photo-anodic current for the TiO₂ photo-anode. The photo-electrocatalytic performance of Sb₂S₃/TiO₂ photo-anode would be further improved by adding Co²⁺ ions in the electrolyte solution due to low recombination rates of charge carriers and facilitated electron transfers.

Author Contributions: Conceptualization, D.L. and F.H.; methodology, F.H.; investigation and data curation, M.M.A. and F.H.; formal analysis, S.M. and F.H.; supervision, D.L.; writing—original draft preparation, F.H.; writing—review and editing, D.L. and Z.Y. All authors have read and agreed to the published version of the manuscript.

Funding: This project was supported by the Natural Science Foundation of Ningxia Province, grant number 2021AAC03170.

Institutional Review Board Statement: Not applicable.

Informed Consent Statement: Not applicable.

Data Availability Statement: Not applicable.

Acknowledgments: F.H. thanks Hefei University of Technology for providing with a Ph.D. D.L. thanks the Natural Science Foundation of Ningxia Province (Grant No. 2021AAC03170).

Conflicts of Interest: The authors declare no conflict of interest.

References

1. Grätzel, M. Photoelectrochemical cells. *Nature* **2001**, *414*, 338–344. [[CrossRef](#)] [[PubMed](#)]
2. Kment, S.; Riboni, F.; Pausova, S.; Wang, L.; Wang, L.; Han, H.; Hubicka, Z.; Krysa, J.; Schmuki, P.; Zboril, R. Photoanodes based on TiO₂ and α -Fe₂O₃ for solar water splitting—superior role of 1D nanoarchitectures and of combined heterostructures. *Chem. Soc. Rev.* **2017**, *46*, 3716–3769. [[CrossRef](#)] [[PubMed](#)]
3. Kudo, A.; Miseki, Y. Heterogeneous photocatalyst materials for water splitting. *Chem. Soc. Rev.* **2009**, *38*, 253–278. [[CrossRef](#)] [[PubMed](#)]
4. Fujishima, A.; Honda, K. Electrochemical Photolysis of Water at a Semiconductor Electrode. *Nature* **1972**, *238*, 37–38. [[CrossRef](#)]
5. Chandra, D.; Tsuruya, R.; Sato, T.; Takama, D.; Abe, N.; Kajita, M.; Li, D.; Togashi, T.; Kurihara, M.; Saito, K.; et al. Characterization of Interfacial Charge-Transfer Photoexcitation of Polychromium-Oxo-Electrodeposited TiO₂ as an Earth-Abundant Photoanode for Water Oxidation Driven by Visible Light. *ChemPlusChem* **2016**, *81*, 1116–1122. [[CrossRef](#)]
6. El Rouby, W.M.A.; Antuch, M.; You, S.; Millet, P. Surface sensitization of TiO₂ nanorod mats by electrodeposition of ZIF-67 for water photo-oxidation. *Electrochim. Acta* **2020**, *339*, 135882–135897. [[CrossRef](#)]
7. Liu, R.; Fang, S.Y.; Tsai, K.C.; Yang, W.D. Enhancing hydrogen evolution of water splitting under solar spectra using Au/TiO₂ heterojunction photocatalysts. *Int. J. Hydrogen Energy* **2021**, *46*, 28462–28473. [[CrossRef](#)]
8. Park, H.; Choi, W.; Hoffmann, M.R. Effects of the preparation method of the ternary CdS/TiO₂/Pt hybrid photocatalysts on visible light-induced hydrogen production. *J. Mater. Chem.* **2008**, *18*, 2379–2385. [[CrossRef](#)]
9. Gupta, B.; Melvin, A.A.; Matthews, T.; Dash, S.; Tyagi, A.K. TiO₂ modification by gold (Au) for photocatalytic hydrogen (H₂) production. *Renew. Sust. Energ. Rev.* **2016**, *58*, 1366–1375. [[CrossRef](#)]
10. Patra, K.K.; Gopinath, C.S. Harnessing Visible-Light and Limited Near-IR Photons through Plasmon Effect of Gold Nanorod with AgTiO₂. *J. Phys. Chem. C* **2018**, *122*, 1206–1214. [[CrossRef](#)]
11. Ibrahim, O.Y.; Gondal, A.M. Visible-light-driven photocatalytic performance of a Z-scheme based TiO₂/WO₃/g-C₃N₄ ternary heterojunctions. *Mol. Catal.* **2021**, *505*, 111494. [[CrossRef](#)]
12. Ge, M.; Cai, J.; Cao, C.; Huang, J.; Zhang, X.; Shen, J.; Wang, S.; Zhang, S.; Zhang, K.Q.; Lai, Y.; et al. A review of TiO₂ nanostructured catalysts for sustainable H₂ generation. *Int. J. Hydrogen Energy* **2017**, *42*, 8418–8449. [[CrossRef](#)]
13. Chen, S.; Li, C.; Hou, Z. A novel in situ synthesis of TiO₂/CdS heterojunction for improving photoelectrochemical water splitting. *Int. J. Hydrogen Energy* **2019**, *44*, 25473–25485. [[CrossRef](#)]
14. Ding, Q.; Gou, L.; Wei, D.; Xu, D.; Fan, W.; Shi, W. Metal-organic framework derived Co₃O₄/TiO₂ heterostructure nanoarrays for promote photoelectrochemical water splitting. *Int. J. Hydrogen Energy* **2021**, *46*, 24965–24976. [[CrossRef](#)]
15. Int. J. Hydrogen Energy Ismail, M.; Chebaane, M.M.; Bousselmi, L.; Zahraa, O.; Olivier, C.; Toupance, T. Photoelectrochemical properties of WO₃ modified anatase TiO₂ photoanodes and application for dye-sensitized solar cells. *Surf. Interfaces* **2021**, *27*, 101543–101551. [[CrossRef](#)]
16. Le, T.T.T.; Tran, D.T.; Danh, T.H. Remarkable enhancement of visible light driven photocatalytic performance of TiO₂ by simultaneously doping with C, N, and S. *Chem. Phys.* **2021**, *545*, 111144–111153. [[CrossRef](#)]
17. Mollavali, M.; Rohani, S.; Elahifard, M.; Behjatmanesh-Ardakani, R.; Nourany, M. Band gap reduction of (Mo+N) co-doped TiO₂ nanotube arrays with a significant enhancement in visible light photo-conversion: A combination of experimental and theoretical study. *Int. J. Hydrogen Energy* **2021**, *46*, 21475–21498. [[CrossRef](#)]
18. Imran, M.; Saeed, Z.; Pervaiz, M.; Mehmood, K.; Ejaz, R.; Younas, U.; Nadeem, H.A.; Hussain, S. Enhanced visible light photocatalytic activity of TiO₂ co-doped with Fe, Co, and S for degradation of Congo red. *Spectrochim. Acta A Mol. Biomol. Spectrosc.* **2021**, *255*, 119644–119655. [[CrossRef](#)]
19. Cerdan-Pasaran, A.; López-Luke, T.; Mathewa, X.; Mathews, N.R. Effect of cobalt doping on the device properties of Sb₂S₃-sensitized TiO₂ solar cells. *Sol. Energy* **2019**, *183*, 697–703. [[CrossRef](#)]
20. Elbakkay, M.H.; El Rouby, W.M.A.; Mariño-López, A.; Sousa-Castillo, A.; Salgueiriño, V.; El-Dek, S.I.; Farghali, A.A.; Correa Duarte, M.A.; Millet, P. One-pot synthesis of TiO₂/Sb₂S₃/RGO complex multicomponent heterostructures for highly enhanced photoelectrochemical water splitting. *Int. J. Hydrogen Energy* **2021**, *46*, 31216–31227.
21. Ben Naceur, J.; Ouertani, R.; Chakhari, W.; Chtourou, R. Photo-electrochemical properties of Sb₂S₃/TiO₂ heterostructures integrally synthesis by hydrothermal method. *J. Mater. Sci. Mater. Electron.* **2019**, *30*, 5631–5639. [[CrossRef](#)]
22. Ortiz-Bustos, J.; Hierro, I.; de Sánchez-Ruiz, A.; García-Martínez, J.C.; Pérez, Y. Tuning of type-I and type-II mechanisms for visible light degradation in tris(styryl)benzene-sensitized TiO₂ nanoparticles. *Dyes Pigments* **2021**, *18*, 108802–108816. [[CrossRef](#)]
23. Yu, Y.-X.; Yu, Y.X.; Pan, L.; Son, M.K.; Mayer, M.; Zhang, W.D.; Hagfeldt, A.; Luo, J.; Grätzel, M. Solution Processed Cu₂S Photocathodes for Photoelectrochemical Water Splitting. *ACS Energy Lett.* **2018**, *3*, 760–766. [[CrossRef](#)]
24. Chandra, M.; Bhunia, K.; Pradhan, D. Controlled Synthesis of CuS/TiO₂ Heterostructured Nanocomposites for Enhanced Photocatalytic Hydrogen Generation through Water Splitting. *Inorg. Chem.* **2018**, *57*, 4524–4533. [[CrossRef](#)]
25. Hou, Y.; Li, X.; Zhao, Q.; Quan, X.; Chen, G. Fabrication of Cu₂O/TiO₂ nanotube heterojunction arrays and investigation of its photoelectrochemical behavior. *App. Phys. Lett.* **2009**, *95*, 093108. [[CrossRef](#)]
26. Zaban, A.; Micić, O.; Gregg, B.A.; Nozik, A. Photosensitization of Nanoporous TiO₂ Electrodes with InP Quantum Dots. *Langmuir* **1998**, *14*, 3153–3156. [[CrossRef](#)]
27. Li, Q.; Zheng, M.; Zhang, B.; Zhu, C.; Wang, F.; Song, J.; Zhong, M.; Ma, L.; Shen, W. InP nanopore arrays for photoelectrochemical hydrogen generation. *Nanotechnology* **2016**, *27*, 075704–075715. [[CrossRef](#)]

28. Wang, T.; Gong, J. Single-Crystal Semiconductors with Narrow Band Gaps for Solar Water Splitting. *Angew. Chem. Int. Edit.* **2015**, *54*, 10718–10732. [[CrossRef](#)]
29. Luo, Z.; Wang, T.; Zhang, J.; Li, C.; Li, H.; Gong, J. Dendritic Hematite Nanoarray Photoanode Modified with a Conformal Titanium Dioxide Interlayer for Effective Charge Collection. *Angew. Chem. Int. Edit.* **2017**, *56*, 12878–12882. [[CrossRef](#)]
30. Yao, H.; Fu, W.; Yang, H.; Ma, J.; Sun, M.; Chen, Y.; Zhang, W.; Wu, D.; Lv, P.; Li, M. Vertical Growth of Two-Dimensional TiO₂ Nanosheets Array Films and Enhanced Photoelectrochemical Properties Sensitized by CdS Quantum Dots. *Electrochim. Acta* **2014**, *125*, 258–265. [[CrossRef](#)]
31. Sharma, V.; CDakshinamurthy, A.; Pandey, B.; Roy, S.C.; Sudakar, C. Highly efficient photoelectrochemical ZnO and TiO₂ nanorod/Sb₂S₃ heterostructured photoanodes through one step thermolysis of Sb-MPA complex. *Sol. Energy* **2021**, *225*, 333–343. [[CrossRef](#)]
32. Zhong, J.S.; Wang, Q.Y.; Liang, H.; Chen, D.Q.; Ji, Z.G. Improving the visible light photocatalytic activity of TiO₂ nanotubes upon decoration with Sb₂S₃ microcrystalline. *Mater. Charact.* **2015**, *109*, 95–99. [[CrossRef](#)]
33. Chang, J.A.; Im, S.H.; Lee, Y.H.; Kim, H.J.; Lim, C.S.; Heo, J.H.; Seok, S.I. Panchromatic photon-harvesting by hole-conducting materials in inorganic-organic heterojunction sensitized-solar cell through the formation of nanostructured electron channels. *Nano Lett.* **2012**, *12*, 1863–1867. [[CrossRef](#)] [[PubMed](#)]
34. Maiti NIm, S.H.; Lima, C.-S.; Seok, S.I. A chemical precursor for depositing Sb₂S₃ onto mesoporous TiO₂ layers in nonaqueous media and its application to solar cells. *Dalton Trans.* **2012**, *41*, 11569–11572. [[CrossRef](#)]
35. Zhu, G.; Pan, L.; Xu, T.; Sun, Z. One-step synthesis of CdS sensitized TiO₂ photoanodes for quantum dot-sensitized solar cells by microwave assisted chemical bath deposition method. *Acs Appl. Mater. Inter.* **2011**, *3*, 1472–1478. [[CrossRef](#)]
36. Itzhaik, Y.; Itzhaik, Y.; Niitsoo, O.; Page, M.G.; Hodes, G. Sb₂S₃-Sensitized Nanoporous TiO₂ Solar Cells. *J. Phys. Chem. C* **2013**, *113*, 4254–4256. [[CrossRef](#)]
37. Sharavath, V.; Sarkar, S.; Ghosh, S. One-pot hydrothermal synthesis of TiO₂/graphene nanocomposite with simultaneous nitrogen-doping for energy storage application. *J. Electroanal. Chem.* **2018**, *829*, 208–216. [[CrossRef](#)]
38. Chen, L.; Zhu, W.; Han, Q.; Yang, X.; Lu, L.; Wang, X. Preparation of rod-like Sb₂S₃ dendrites processed in conventional hydrothermal. *Mater. Lett.* **2009**, *63*, 1258–1261. [[CrossRef](#)]
39. Parize, R.; Cossuet, T.; Chaix-Pluchery, O.; Roussel, H.; Appert, E.; Consonni, V. In situ analysis of the crystallization process of Sb₂S₃ thin films by Raman scattering and X-ray diffraction. *Mater. Design* **2017**, *121*, 1–10. [[CrossRef](#)]
40. Kozytskiy, A.V.; Stroyuk, O.L.; Skoryk, M.A.; Dzhagan, V.M.; Kuchmiy, S.Y.; Zahn, D.R.T. Photochemical formation and photoelectrochemical properties of TiO₂/Sb₂S₃ heterostructures. *J. Photochem. Photobiol. A* **2015**, *303–304*, 8–16. [[CrossRef](#)]
41. Pal, M.; Mathews, N.R.; Mathew, X. Surfactant-mediated self-assembly of Sb₂S₃ nanorods during hydrothermal synthesis. *J. Mater. Res.* **2017**, *32*, 530–538. [[CrossRef](#)]
42. Avilez Garcia, R.G.; Meza Avedaño, C.A.; Pal, M.; Paraguay Delgado, F.; Mathews, N.R. Antimony sulfide (Sb₂S₃) thin films by pulse electrodeposition: Effect of thermal treatment on structural, optical and electrical properties. *Mat. Sci. Semicon. Proc.* **2016**, *44*, 91–100. [[CrossRef](#)]
43. Lou, W.; Chen, M.; Wang, X.; Liu, W. Novel Single-Source Precursors Approach to Prepare Highly Uniform Bi₂S₃ and Sb₂S₃ Nanorods via a Solvothermal Treatment. *Chem. Mater.* **2007**, *19*, 872–878. [[CrossRef](#)]
44. Ota, J.; Srivastava, S.K. Tartaric Acid Assisted Growth of Sb₂S₃ Nanorods by a Simple Wet Chemical Method. *Cryst. Growth Des.* **2007**, *7*, 343–347. [[CrossRef](#)]
45. Kay, A.; Cesar, I.; Grätzel, M. New Benchmark for Water Photooxidation by Nanostructured α -Fe₂O₃ Films. *J. Am. Chem. Soc.* **2006**, *128*, 15714–15721. [[CrossRef](#)]
46. Li, D.; Takeuchi Ryouchi Chandra, D.; Saito, K.; Yui, T.; Yagi, M. Visible Light-Driven Water Oxidation on an In Situ N₂-Intercalated WO₃ Nanorod Photoanode Synthesized by a Dual-Functional Structure-Directing Agent. *ChemSusChem* **2018**, *11*, 1151–1156. [[CrossRef](#)]